THE EARLIEST NEAR-INFRARED TIME-SERIES SPECTROSCOPY OF A TYPE Ia SUPERNOVA

E. Y. Hsiao[1], G. H. Marion[2], M. M. Phillips[1], C. R. Burns[3], C. Winge[4], N. Morrell[1], C. Contreras[1], W. L. Freedman[3],
M. Kromer[5], E. E. E. Gall[5,6], C. L. Gerardy[7], P. Höflich[7], M. Im[8], Y. Jeon[8], R. P. Kirshner[2], P. E. Nugent[9,10],
S. E. Persson[3], G. Pignata[11], M. Roth[1], V. Stanishev[12], M. Stritzinger[13], and N. B. Suntzeff[14]

[1] Carnegie Observatories, Las Campanas Observatory, Colina El Pino, Casilla 601, Chile; hsiao@lco.cl
[2] Harvard-Smithsonian Center for Astrophysics, 60 Garden Street, Cambridge, MA 02138, USA
[3] Carnegie Observatories, 813 Santa Barbara St, Pasadena, CA 91101, USA
[4] Gemini South Observatory, c/o AURA Inc., Casilla 603, La Serena, Chile
[5] Max-Planck-Institut für Astrophysik, Karl-Schwarzschild-Str. 1, D-85741 Garching bei München, Germany
[6] Astrophysics Research Centre, School of Maths and Physics, Queen's University Belfast, Belfast BT7 1NN, UK
[7] Department of Physics, Florida State University, Tallahassee, FL 32306, USA
[8] CEOU/Astronomy Program, Department of Physics & Astronomy, Seoul National University, Seoul, Republic of Korea
[9] Computational Cosmology Center, Computational Research Division, Lawrence Berkeley National Laboratory, 1 Cyclotron
Road MS 50B-4206, Berkeley, CA 94611, USA
[10] Department of Astronomy, University of California, Berkeley, CA, 94720-3411, USA
[11] Departamento de Ciencias Fisicas, Universidad Andres Bello, Avda. Republica 252, Santiago, Chile
[12] CENTRA - Centro Multidisciplinar de Astrofísica, Instituto Superior Técnico, Av. Rovisco Pais 1, 1049-001 Lisbon, Portugal
[13] Department of Physics and Astronomy, Aarhus University, Ny Munkegade, DK-8000 Aarhus C, Denmark
[14] Department of Physics & Astronomy, Mitchell Institute of Fundamental Physics & Astronomy,
Texas A&M University, College Station, TX 77843, USA

ABSTRACT

We present ten medium-resolution, high signal-to-noise ratio near-infrared (NIR) spectra of SN 2011fe from SpeX on the NASA Infrared Telescope Facility (IRTF) and Gemini Near-Infrared Spectrograph (GNIRS) on Gemini North, obtained as part of the Carnegie Supernova Project. This data set constitutes the earliest time-series NIR spectroscopy of a Type Ia supernova (SN Ia), with the first spectrum obtained at 2.58 days past the explosion and covering -14.6 to $+17.3$ days relative to B-band maximum. C I $\lambda 1.0693\ \mu$m is detected in SN 2011fe with increasing strength up to maximum light. The delay in the onset of the NIR C I line demonstrates its potential to be an effective tracer of unprocessed material. For the first time in a SN Ia, the early rapid decline of the Mg II $\lambda 1.0927\ \mu$m velocity was observed, and the subsequent velocity is remarkably constant. The Mg II velocity during this constant phase locates the inner edge of carbon burning and probes the conditions under which the transition from deflagration to detonation occurs. We show that the Mg II velocity does not correlate with the optical light-curve decline rate $\Delta m_{15}(B)$. The prominent break at $\sim 1.5\ \mu$m is the main source of concern for NIR k-correction calculations. We demonstrate here that the feature has a uniform time evolution among SNe Ia, with the flux ratio across the break strongly correlated with $\Delta m_{15}(B)$. The predictability of the strength and the onset of this feature suggests that the associated k-correction uncertainties can be minimized with improved spectral templates.

Key words: cosmology: observations – infrared: general – supernovae: general – supernovae: individual
(SN 2011fe)

Online-only material: color figures

1. INTRODUCTION

Type Ia supernovae (SNe Ia) provide a direct measure of the expansion history of the universe and have led to the discovery of the accelerated expansion (Riess et al. 1998; Perlmutter et al. 1999). The unknown cause of the accelerated expansion is commonly referred to as "dark energy." Although SNe Ia remain the most proven technique for studying dark energy, there are legitimate concerns that systematic errors coming from the astrophysics of SNe Ia will ultimately limit their accuracy.

Fortunately, observations in the NIR offer a way forward. Elias et al. (1985) presented the first SN Ia NIR Hubble diagram with a dispersion of only 0.2 mag. Subsequent studies indicated that NIR peak luminosity indeed show a smaller intrinsic scatter than that in the optical (e.g., Krisciunas et al. 2004; Wood-Vasey et al. 2008; Folatelli et al. 2010; Barone-Nugent et al. 2012), a result that was supported by the theoretical work of Kasen (2006). As opposed to the width-luminosity relation in the optical (Phillips 1993), NIR peak luminosities for all except the fastest-declining events have only a slight dependence on the

light-curve shape (Krisciunas et al. 2009; Kattner et al. 2012). Further analyses confirmed that NIR luminosities without light-curve shape corrections are more effective distance indicators than corrected optical luminosities (Mandel et al. 2009, 2011). A key ingredient to realize the full potential of NIR SN Ia cosmology is NIR spectroscopy, such that the peak luminosities can be accurately k-corrected to the rest frame. With the limited scope and size of the world's current NIR spectroscopic sample, to date the time evolution and the diversity of the spectral features are poorly understood. These uncertainties directly affect the determination of the NIR rest-frame peak luminosities.

Given that SNe Ia play a critical role in observational cosmology, it is as critical as ever to understand the explosion mechanisms and the progenitor systems. NIR spectra also provide several key diagnostics of SN Ia physics. The C I $\lambda 1.0693\ \mu$m line is strong and isolated in the NIR and is an ideal tracer of primordial, unprocessed material from the carbon-oxygen white dwarf (Marion et al. 2006). The amount and the distribution of unprocessed material are key discriminators for SN Ia explosion models. Magnesium is a product of explosive carbon burning and

Table 1
List of Observations

UT Date	UT MJD	Instrument	Phase wrt Explosion	Phase wrt B Maximum	Number of Exposures	Integration Time	SN 2011fe Air Mass	Telluric Standard	Telluric Air Mass
2011 Aug 26	55799.27	SpeX	2.58 d	−14.6 d	8	1200 s	2.00	HD143187	1.92
2011 Aug 28	55801.25	GNIRS	4.56 d	−12.6 d	8	2400 s	1.78	HIP69366	1.91
2011 Aug 31	55804.23	GNIRS	7.55 d	−9.7 d	8	960 s	1.77	HIP69366	1.77
2011 Sep 3	55807.24	GNIRS	10.55 d	−6.7 d	8	1200 s	1.89	HIP69366	2.05
2011 Sep 7	55811.11	GNIRS	14.42 d	−2.8 d	8	960 s	1.88	HIP69366	1.99
2011 Sep 10	55814.21	GNIRS	17.52 d	+0.3 d	8	960 s	1.87	HIP69366	1.95
2011 Sep 13	55817.24	GNIRS	20.55 d	+3.3 d	8	960 s	2.28	HIP69366	2.62
2011 Sep 18	55822.13	GNIRS	25.45 d	+8.2 d	8	700 s	2.25	HIP69366	2.54
2011 Sep 22	55826.22	GNIRS	29.53 d	+12.3 d	8	960 s	2.35	HIP69366	2.84
2011 Sep 27	55831.21	GNIRS	34.52 d	+17.3 d	8	960 s	2.54	HIP72520	2.35

Note. The time of explosion of MJD 55796.687 (Nugent et al. 2011) and the time of B-band maximum of MJD 55813.9 (Vinkó et al. 2012) were adopted.

not oxygen burning. The strong NIR Mg II $\lambda 1.0927$ μm line provides a direct measure of the inner boundary of carbon burning and probes the conditions under which transition from deflagration to detonation occurs (Wheeler et al. 1998). After maximum light, the dramatic drop in electron scattering opacity, coupled with heavy line blanketing from fully-processed iron-peak material, rapidly forms the prominent feature at 1.5–1.9 μm and provides a temperature probe of the line blanketing material (Wheeler et al. 1998).

With the advent of NIR narrow-gap semiconductor detectors, pioneering studies of SN Ia NIR spectroscopy began in the late 1980s (e.g., Frogel et al. 1987; Lynch et al. 1990; Spyromilio et al. 1992, 1994). Bowers et al. (1997) published the first multi-object sample, which consisted of NIR spectra taken in late and nebular phases. The current sample of SN Ia NIR spectroscopy largely consists of data of a few nearby SNe Ia. We list here the spectra included in our analysis: SNe 1994D (Meikle et al. 1996), 1998bu (Jha et al. 1999; Hernandez et al. 2000; Hamuy et al. 2002), 1999by (Höflich et al. 2002), 1999ee (Hamuy et al. 2002), 2002bo (Benetti et al. 2004), 2002dj (Pignata et al. 2008), 2003du (Stanishev et al. 2007), 2004S (Krisciunas et al. 2007), 2005cf (Gall et al. 2012), 2011iv (Foley et al. 2012). Marion et al. (2003, 2009) published a catalog of 41 SN Ia near-infrared spectra, nearly doubling the world's sample. Owing to these works, we can begin to examine the statistical spectroscopic properties of SNe Ia in the NIR.

Despite the progress made thus far, the NIR spectroscopic sample of SNe Ia is not yet ideal. The NIR sample size is two orders of magnitude smaller than that in the optical. Many of the SNe Ia observed lack accompanying photometric information. Most importantly, there has only been a handful of time-series observations. Densely-sampled time-series observations are required to understand how the features evolve with time and vary among object-to-object. The discovery of the nearby SN 2011fe made possible such observations.

On 2011 August 24, SN 2011fe was detected within hours of its explosion in M101 (Nugent et al. 2011). Its proximity and early detection provided a unique opportunity to make exquisitely detailed observations of a SN Ia. SN 2011fe has reportedly representative properties of SNe Ia and serves as an ideal baseline to compare to other objects. It is rapidly becoming the best-studied SN Ia to date, with numerous studies from X-ray to radio already published (e.g., Li et al. 2011; Bloom et al. 2012; Horesh et al. 2012; Röpke et al. 2012; Chomiuk et al. 2012; Margutti et al. 2012; Parrent et al. 2012; Brown et al. 2012; Matheson et al. 2012; Vinkó et al. 2012; Patat et al. 2013). Early light curves and pre-explosion images of SN 2011fe placed

strong constraints on the progenitor system, ruling out a massive companion star, disfavoring most theoretical double-degenerate progenitor systems, and excluding Roche-Lobe overflowing red giant and main-sequence companions to high significance (Nugent et al. 2011; Li et al. 2011; Bloom et al. 2012); although, a M dwarf companion may evade these constraints (Wheeler 2012). Ten NIR spectra of SN 2011fe were obtained in the span of a month, as part of a joint Carnegie Supernova Project (CSP)-CfA Supernova Group program to obtain a statistical sample of NIR spectroscopic observations of supernovae (M. M. Phillips et al., in preparation). The SN 2011fe data set constitutes the earliest and highest signal-to-noise ratio time-series NIR spectroscopy of a SN Ia. In this paper, we present several analyses and insights on time evolution, which would not have been possible without this one-of-a-kind data set.

2. OBSERVATION AND REDUCTION

Only 2.58 days past the explosion, the first NIR spectrum of SN 2011fe was obtained with the SpeX spectrograph (Rayner et al. 2003) on IRTF. Nine subsequent NIR spectra were obtained with a regular three-day cadence with GNIRS (Elias et al. 1998) on Gemini North. Relatively short per-frame exposure times were chosen to prevent the saturation of the telluric OH lines and the supernova. The object was nodded along the slit using the classical ABBA technique. Two ABBA sequences (eight exposures) were obtained at each epoch. To correct the science spectra for the effect of telluric atmospheric absorption, an A0V star was observed at a similar air mass to that of the science observation. The slit was oriented along the parallactic angle for all observations (Filippenko 1982). The spectra from both SpeX and GNIRS presented here have similar medium spectral resolving power of $R \sim$ 1000–2000. With the exception of the first SpeX spectrum, all of the resulting spectra have very high signal-to-noise ratio of well above 100. A journal of the spectroscopic observations is given in Table 1.

The SpeX spectrum was obtained in the cross-dispersed mode, utilizing a grating and prism cross-dispersers, with a 0″.5 slit. This configuration yields a wavelength coverage from 0.8 to 2.5 μm divided over six orders, with gaps over the regions of strong telluric absorptions between the *JHK* bands. With the choice of the 0″.5 slit width, the resulting spectral resolution is in the range of ∼1600–2000. The data were calibrated and reduced using the IDL pipeline Spextool (Cushing et al. 2004), specifically designed for the reduction of SpeX data. The pipeline performed steps of pair subtraction, flat-fielding, aperture definition, spectral tracing and extraction, and wavelength

calibration. The one-dimensional spectra from separate exposures were then combined. Corrections for telluric absorption were performed using the IDL tool xtellcor developed by Vacca et al. (2003). To construct a telluric correction spectrum free of stellar absorption features, a model spectrum of Vega was used to match and remove the hydrogen lines of Paschen and Brackett series from the AV0 telluric standard. The resulting telluric correction spectrum was also used for the absolute flux calibration, as the NIR continua of A0V stars are reasonably approximated by a blackbody, with the temperature (typically ~10,000 K) determined by the color of the star.

The GNIRS spectra were observed in the cross-dispersed mode, in combination with the short-wavelength camera, a 32 lines per mm grating and a 1″.0 slit. This configuration allows for a wide continuous wavelength coverage from 0.8 to 2.5 μm, divided over six orders. Because of the choice of the 1″.0 slit width, the resulting spectral resolution is lower than the SpeX spectrum and in the range of ~1000–1300. The GNIRS data were calibrated and reduced using the gnirs pipeline within the Gemini IRAF[15] package, specifically developed for the reduction of GNIRS data. The steps began with non-linearity correction, locating the spectral orders and flat-fielding. Sky subtractions were performed for each AB pair closest in time, then the two-dimensional spectra were stacked. Spatial distortion correction and wavelength calibrations were applied before the one-dimensional spectrum was extracted. To perform telluric correction, the stellar hydrogen lines were first removed from the telluric star spectrum. The IRAF task telluric was then used to interactively adjust the relative wavelength shift and flux scale to divide out telluric features present in the science spectrum. A blackbody spectrum is then assumed for the telluric star for the flux calibration. Some high-frequency pattern noise with pixel-wide correlations were evident in isolated regions of the spectrum; this is a known issue for the GNIRS detector. These were removed with a low-pass filter. There were adequate overlaps between orders to join the spectra; however, some overlaps occurred in the uncertain regions of strong telluric absorptions between the *JHK* bands. We used the *JHK* photometry of Matheson et al. (2012) as a guide to scale the relative flux before joining the spectral orders.

3. NIR SPECTRA OF SN 2011fe

Ten NIR spectra of SN 2011fe are presented in Figure 1. The early NIR spectra are dominated by electron scattering with the continua resembling the Rayleigh-Jeans tail of a blackbody. The spectral slope remains quite constant until around maximum light. As the ejecta expands and electron scattering opacity decreases, the continuum drops, and a well-defined photosphere no longer exists. Just past maximum light and at regions of heavy line blanketing by iron-peak elements, the lines are formed at larger effective radii producing features seemingly in emission (Wheeler et al. 1998). The combination of these lines in "emission," and the decreased continuum, forms the most prominent feature in the NIR between 1.5–1.9 μm.

Alternatively, the origin of the increased flux at 1.5–1.9 μm was shown to be caused by increased fluorescence in the region (Gall et al. 2012). Line blanketing of iron-group elements is very efficient in blocking flux in the ultraviolet (UV) part of the spectrum. In contrast, the opacity in the optical and

NIR is significantly lower (e.g., Pinto & Eastman 2000). Thus photons absorbed in the UV and redistributed to the NIR by line fluorescence may escape from the ejecta (Kromer & Sim 2009). At wavelengths where line fluorescence is highly effective, this can lead to an increased flux.

We fit three early NIR spectra with the automated spectrum synthesis code SYNAPPS (Thomas et al. 2011b) derived from SYNOW (Branch et al. 2005). The results are shown in Figure 2. SYNAPPS uses a highly parameterized but fast spectrum synthesis technique, useful for identifying the ions that form the observed features. We included in the fits ions which are commonly identified or expected to be present in normal SN Ia optical and NIR spectra: C I, C II, O I, Mg II, Si II, Si III, S II, Ca II, Fe II, Fe III, Co II, and Ni II. Such an expansive list of ions was included such that SYNAPPS can objectively determine the absence or presence of each ion species. The most prominent features at this epoch are attributed to intermediate-mass species, such as O I, Mg II, and Si III. The strong Mg II $\lambda1.0927\,\mu$m absorption is formed at a relatively isolated region near 1.05 μm. Signatures of unburned C I were detected and will be discussed in detail in Section 4.1. Redward of the strong Mg II line near 1.05 μm, four absorption features from 1.1 μm to 1.4 μm were identified as O I/Si III, C I/Ca II, Si III, and Si III, respectively.

In terms of iron-peak elements, SYNAPPS interprets the strong feature near 1.6 μm as Fe III. This feature was identified as Mg II/Si II/Co II by Marion et al. (2009) and Si II by Wheeler et al. (1998) and Gall et al. (2012). Two absorption minima near 1.6 μm were resolved in SN 2011fe. Both minima are attributed to Fe III with weaker influences from Mg II, Si II, and Si III in the redder of the two absorptions. The Fe III interpretation also yielded good fits for several other features in and around the *H* band (Figure 2). Ni II appears to be weak in all three early spectra, while Co II increases in strength with time. The increasing influence of Co II is attributed to both decreasing opacity and increasing abundance of ^{56}Co from the radioactive decay of ^{56}Ni.

The presence or absence of a certain ionization stage of a species is regulated by the combination of temperature and the strength of the lines in question. While C II was positively identified in the optical spectra of SN 2011fe (Parrent et al. 2012), the C II lines are weak in the NIR. Instead, C I is identified in the NIR, with the strongest influence near maximum light rather than at earlier phases (Section 4.1). While Si II is the hallmark feature of a SN Ia in the optical, Si III was found to have more identifiable features in the NIR spectra of SN 2011fe. At early phases, Fe III has stronger influences than Fe II in the NIR, similar to the behavior in the optical.

Recently, Gall et al. (2012) showed the close resemblance between the NIR spectra of SN 2005cf and the synthetic spectra of the hydrodynamical explosion model W7 (Nomoto et al. 1984; Iwamoto et al. 1999). They found that in the NIR, the emerging flux is almost entirely due to fluorescent emission with a few features formed by strong P-Cygni absorptions. Here, we make the comparison with the NIR spectra of SN 2011fe, using the same synthetic spectra without modifications (Figure 3). While SYNAPPS is useful for identifying the line forming ion species, it does not provide detailed post-processing of stellar explosion models. The W7 model spectra in Figure 3 were calculated using the Monte Carlo radiative transfer code ARTIS (Kromer & Sim 2009). It provides a fully self-consistent solution to the radiative transfer problem and produces time-dependent spectral synthesis without any free parameters. As was found by Gall et al. (2012), the spectral features of

---
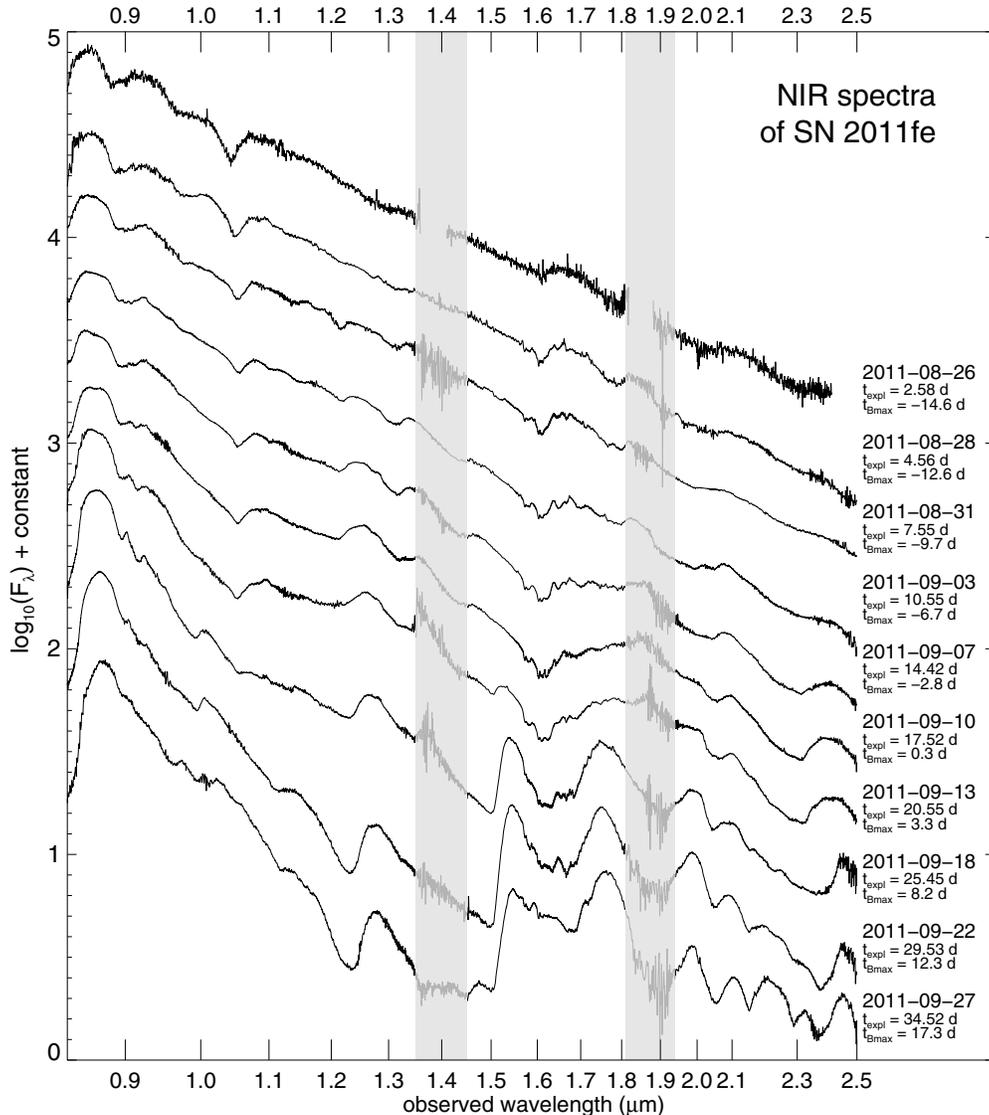
Figure 1. NIR spectra of SN 2011fe. The wavelength is as observed. The logarithmic scale of flux is plotted. For clarity, the spectra are scaled such that they have constant spacing at 1 μm. The UT date of observation, phase relative to explosion and phase relative to B-band maximum are labeled for each spectrum. The gray vertical bands mark the regions of the strongest telluric absorptions.

the observed and model spectra show encouraging similarities. A few differences are noted here. Slight discrepancy is observed in the time evolution of the NIR brightness. The two spectra of SN 2011fe near a month past explosion or 10 days after B-band maximum are consistently fainter than the model spectra. The strong Mg II $\lambda 1.0927$ μm feature near 1.05 μm is present in the early model spectra; however, discrepancies in the velocity evolution are evident between the observed and model spectra. While the Mg II $\lambda 1.0927$ μm velocity of SN 2011fe decreases rapidly (Section 4.2), the velocity in the model spectra remains high. Also, the observed strong break near 1.5 μm (Section 4.3), one of the most prominent spectral features in the NIR, is not reproduced by the model until approximately one month past the explosion. Even then, the velocity of the feature does not match the observations.

## 4. DIAGNOSTICS OF SN Ia PHYSICS

There is currently no full theoretical description of the explosion mechanism of SNe Ia that accounts for the observed diversity. In the most established model, carbon is ignited near

the center of a carbon-oxygen white dwarf, as it approaches the Chandrasekhar mass (Hoyle & Fowler 1960). The initial thermonuclear carbon burning starts in a subsonic deflagration (Nomoto et al. 1976). To produce partially-processed, intermediate-mass material observed in SNe Ia, the transition to detonation is "delayed," such that the white dwarf is able to expand appreciably to allow for partial burning. A possible transition to a supersonic detonation then rapidly incinerates the star (Khokhlov 1991; Yamaoka et al. 1992). While some mechanisms for the transition from deflagration in the carbon flame to the subsequent detonation in the oxygen flame have been proposed, its nature remains uncertain and controversial (e.g., Khokhlov et al. 1997; Niemeyer & Woosley 1997; Plewa et al. 2004; Aspden et al. 2008; Woosley et al. 2009, 2011). The conditions under which the transition occurs are still essentially treated as free parameters within models.

Early NIR spectra provide several powerful diagnostics of the physics of SN Ia explosions, and can serve as discriminators for competing explosion models. Since magnesium is a product of explosive carbon burning and not oxygen burning, the NIR Mg II lines provide a direct measure of the inner boundary
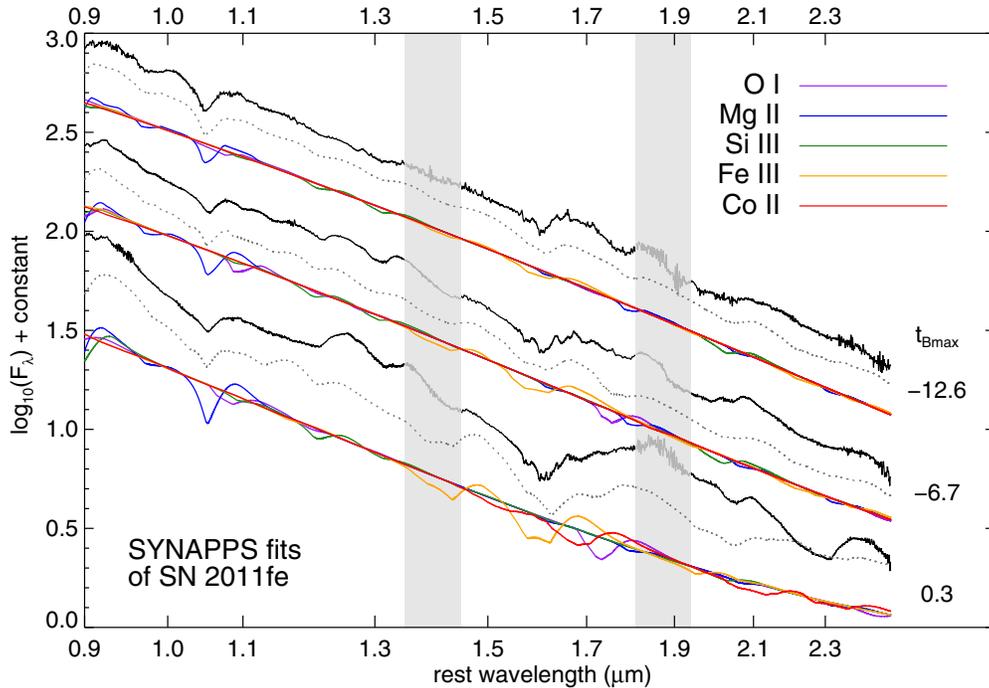
Figure 2. SYNAPPS fits for three early NIR spectra of SN 2011fe. The observed spectra and the SYNAPPS fits are plotted in black solid and gray dotted curves, respectively. The colored curves show individual contributions from the most prominent ions. The wavelength axis is plotted in the rest frame of the host galaxy. The phase relative to B-band maximum is labeled for each spectrum.
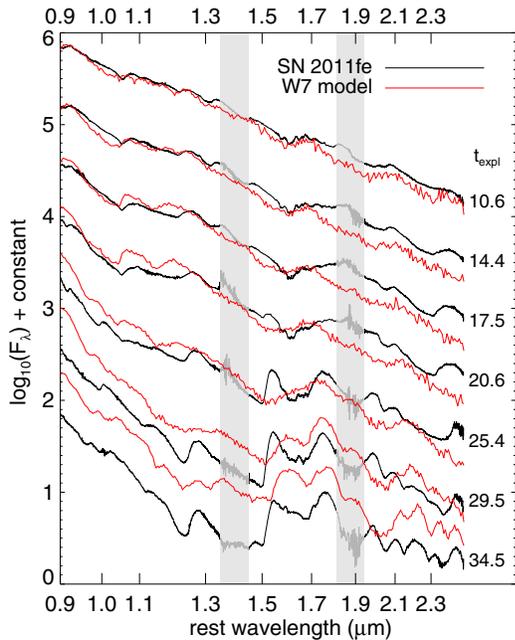
Figure 3. Comparison between the synthetic W7 model spectra and the NIR spectra of SN 2011fe. The model spectra were calculated using the radiative transfer code ARTIS for the W7 model. The observed and the model spectra are plotted in black and red, respectively. The wavelength axis is plotted in the rest frame of the host galaxy of SN 2011fe. The absolute flux scales of the observed and model time series were matched at the first comparison epoch, then the same offset was applied to each subsequent pair of spectra. The phase relative to explosion is labeled for each spectrum.

et al. 1995, 2002). The presence or absence of unprocessed material is one of the key predictions of SN Ia explosion models. The NIR C I lines provide an independent confirmation of the findings from the intensively-studied optical C II lines. Past maximum light, the continuum opacity from electron scattering decreases dramatically. Coupled with heavy line blanketing from fully-processed, iron-peak material, the NIR spectrum probes a large range of depths and the temperature of the line blanketing material (Wheeler et al. 1998). In this section, we present several techniques to quantify the characteristics of NIR spectra and discuss the use of these measurements as various diagnostics of SN Ia physics.

4.1. Unburned Carbon

Since oxygen is also produced from carbon burning, carbon provides the most direct probe of the primordial material from the progenitor carbon-oxygen white dwarf. The quantity, distribution, and incidence of unburned carbon in SNe Ia provide important constraints for explosion models. Turbulent deflagration models predict that a large amount of unprocessed carbon should be left over (Gamezo et al. 2003; Röpke et al. 2007). In general, a transition to detonation would result in complete carbon burning (Höflich et al. 2002; Marion et al. 2006; Kasen et al. 2009); although, exceptions have been found. For the lowest transition density in a grid of delayed detonation models, both the model and the observations of SN 1999by showed strong C I signatures (Höflich et al. 2002), but SN 1999by is significantly subluminous (Toth & Szabó 2000) and not representative of a normal SN Ia. Gamezo et al. (2004) showed that pockets of cool and dense unburned material could be pulled down toward the center and escape the detonation wave.

Unburned carbon in SNe Ia has been the subject of several intensive studies in recent years. Examining the C I lines in NIR spectra of three normal SNe Ia without the aid of spectrum
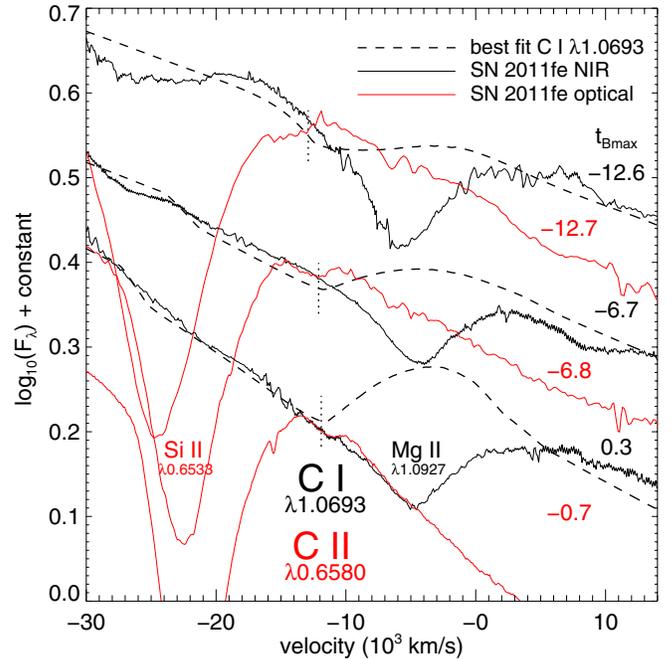
of carbon burning, and could place meaningful constraints on the conditions under which the transition to detonation occurs (Wheeler et al. 1998). The location of the boundary is also particularly sensitive to the transition density, which is inextricably linked to the amount of ^{56}Ni produced (e.g., Höflich
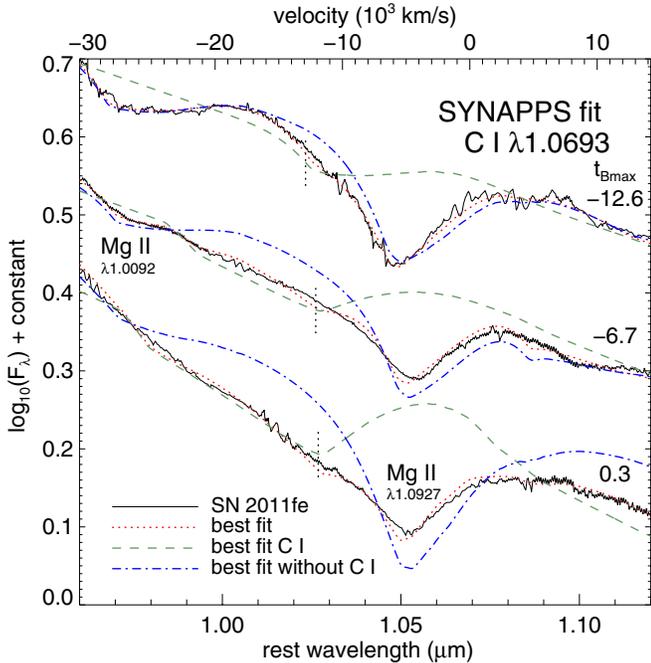
Figure 4. SYNAPPS fits of three early NIR spectra of SN 2011fe in the region of the C I $\lambda1.0693\,\mu$m line. The velocity axis is plotted with respect to the rest wavelength of C I $\lambda1.0693\,\mu$m. The spectra are plotted as solid black curves. The best-fit synthesized spectra are plotted as follows: with all ions, with only C I, and with all ions except C I. These are plotted as red dotted, green dashed, and blue dash-dotted curves, respectively. The vertical dotted lines mark the location of the best-fit minimum photospheric velocity. The phases relative to B-band maximum light are noted.

(A color version of this figure is available in the online journal.)

Figure 5. Comparison of the NIR C I $\lambda1.0693\,\mu$m and the optical C II $\lambda0.6580\,\mu$m lines of SN 2011fe in velocity space. The velocity axis is plotted with respect to the rest wavelength of the C I $\lambda1.0693\,\mu$m and C II $\lambda0.6580\,\mu$m lines. The NIR spectra are plotted as black curves. The optical spectra are taken from Parrent et al. (2012) and plotted as red curves. The C I profiles from the best-fit synthesized spectra are plotted as black dashed curves. The vertical dotted lines mark the location of the best-fit minimum photospheric velocity. The phases relative to B-band maximum light for the NIR and optical spectra are labeled in black and red, respectively.

(A color version of this figure is available in the online journal.)

synthesis techniques, Marion et al. (2006) concluded that the abundance of unprocessed material is low. Thomas et al. (2007) presented the most convincing detection of the C II $\lambda0.6580\,\mu$m feature in the early optical spectra of SN 2006D. In subsequent studies with larger optical spectroscopic samples, 20%–30% of the early spectra were found to show C II signatures (Thomas et al. 2011a; Parrent et al. 2011; Folatelli et al. 2012; Silverman & Filippenko 2012). Several studies have noted that this fraction represents the lower limit, as noise, velocity blueshift, and the phase at which the SNe Ia were followed up could affect the C II detection (e.g., Branch et al. 2007; Folatelli et al. 2012). The velocities of the detected C II lines are generally low. There have also been hints that SNe Ia with detected C II have preferentially bluer colors and narrower light curves (Thomas et al. 2011a; Folatelli et al. 2012), but this finding was not held up in the examinations of other data sets (e.g., Blondin et al. 2012; Parrent et al. 2011). Nonetheless, there appears to be a consensus that the mass fraction of the photospheric carbon is low (e.g., Branch et al. 2003; Marion et al. 2006; Thomas et al. 2007; Tanaka et al. 2008).

The automated spectrum synthesis code SYNAPPS has been employed successfully to identify the C II $\lambda0.6580\,\mu$m lines in early optical spectra (Thomas et al. 2007, 2011a; Parrent et al. 2012). Here we concentrate on the study of the strongest C I line in the NIR at $1.0693\,\mu$m using SYNAPPS. The weaker C I lines are included in the fit, but are heavily blended and more difficult to detect. For example, the C I $\lambda\lambda0.9087, 1.1756\,\mu$m lines are both blended with O I, Si III, and Ca II lines. C I $\lambda1.0693\,\mu$m, at the largest expected range of velocities, lies in between the strong Mg II $\lambda1.0927\,\mu$m line, usually blueshifted to $\sim1.05\,\mu$m, and the weaker Mg II $\lambda1.0092\,\mu$m line, usually blueshifted to

$\sim0.97\,\mu$m. The fits were done for three early spectra over the entire NIR wavelength range (Figure 2). The results zoomed in on the region containing the line profiles of C I $\lambda1.0693\,\mu$m are shown in Figure 4. The best-fit synthesized spectra show very close matches to the observed spectra. In the first spectrum, at approximately two weeks before maximum, the C I signature appears weak and was not required to obtain a decent fit in the region. Starting from a week before maximum, the story changes. The profile begins to take on a flattened shape (Figure 4). The presence of C I is now required to suppress the emission component of the Mg II $\lambda1.0092\,\mu$m P-Cygni profile, which is evident at two weeks before maximum. Near maximum light, the profile remains flat, and the influence of C I is even stronger. Our spectrum has a high enough signal-to-noise ratio to resolve the "notch" from C I $\lambda1.0693\,\mu$m near $1.03\,\mu$m. The strengthening of the C I signature with time may be a result of the increasing ionization fraction of C I versus C II, as the ejecta expands and cools. The unburned carbon in these early NIR spectra was detected at velocities consistent with the photospheric velocity of partially and completely synthesized material. The blueshift of the C I line was observed at $12{,}900\,\mathrm{km\,s^{-1}}$ at two weeks before maximum and leveled off at $\sim12{,}000\,\mathrm{km\,s^{-1}}$ from a week before maximum light. Note that in past analyses, the flattened feature has been attributed to an extended wing of Mg II $\lambda1.0927\,\mu$m (e.g., Marion et al. 2009). This is produced by a detonation front that leads to partial burning up to very high velocities (Höflich et al. 2002).

Our fits were performed without assuming any initial conditions based on the results from the optical, such as strength and velocity. In Figure 5, the C I $\lambda1.0693\,\mu$m feature from the
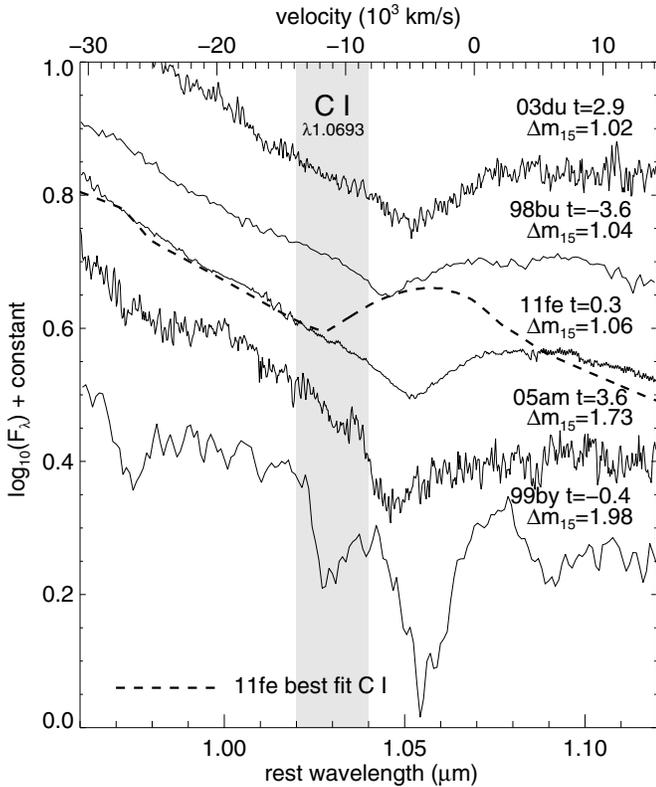
Figure 6. Comparison of the NIR C I $\lambda 1.0693\,\mu$m profile for five SNe Ia near maximum light. The velocity axis is plotted with respect to the rest wavelength of C I $\lambda 1.0693\,\mu$m. The C I profile from the best-fit synthesized spectrum of SN 2011fe is plotted as a black dashed curve. The time of B-band maximum and B-band light-curve decline rate $\Delta m_{15}(B)$ of the literature spectra were taken from Hicken et al. (2009). The phase relative to B-band maximum and $\Delta m_{15}(B)$ are noted for each spectrum.

NIR and C II $\lambda 0.6580\,\mu$m feature from the optical of SN 2011fe are compared in velocity space. Optical spectra taken at phases closest to those of the NIR spectra are shown. The C II features were positively identified in the early optical spectra of SN 2011fe and showed decreasing strength with time (Parrent et al. 2012). The velocities of the C I and C II features match exceptionally well, indicating that these signatures are from the same line-forming material. The interpretation from SYNAPPS that C I $\lambda 1.0693\,\mu$m is the source of the flattened profile on the emission wing of the Mg II $\lambda 1.0092\,\mu$m P-Cygni profile appears to be correct.

It is worth noting here that the flattened profile near $1.03\,\mu$m is a common feature for brighter and slower-declining SNe Ia near maximum light (Figure 6). For fainter, faster-declining SNe Ia, the C I signatures appear to be stronger and easily detectable at maximum light. SN 1999by is the extreme of this example with the conspicuous presence of the C I line. This effect is reminiscent of the familiar sequence of the Si II $\lambda 0.5972\,\mu$m strength (Nugent et al. 1995). It is possible to interpret from these observations that the majority of SNe Ia, at both ends of the brightness extreme, harbor some unprocessed carbon deep in the ejecta. Such a conclusion is discrepant from the 20%–30% found by recent optical studies (e.g., Thomas et al. 2011a; Folatelli et al. 2012; Silverman & Filippenko 2012); although, there are indications that the fraction of detection is higher with earlier spectra (e.g., Folatelli et al. 2012). Since the finding of ubiquitous unprocessed carbon would have profound

implications for our understanding of SN Ia explosions, a larger NIR sample and further studies are warranted for such a claim.

Nonetheless, we have shown here that the C I $\lambda 1.0693\,\mu$m feature in the NIR is potentially a better tracer of unprocessed material than C II $\lambda 0.6580\,\mu$m in the optical. While the signature of C II $\lambda 0.6580\,\mu$m is the strongest between one and two weeks before maximum and fades with time, the influence of C I $\lambda 1.0693\,\mu$m appears to be the strongest at maximum light in SN 2011fe. A change in the ionization condition, as the temperature cools, may have fortuitously brought about a delay in the onset of the C I feature. If this behavior can be verified in other SNe Ia, the problem of the incompleteness of very early optical spectroscopic samples could be circumvented by using a sample of NIR spectra near maximum light. Well situated in a relatively isolated region between the two Mg II lines, the NIR C I line also has the advantage that it is unblended with other strong absorptions for a large range of velocities; while C II $\lambda 0.6580\,\mu$m may be blueshifted into Si II $\lambda 0.6355\,\mu$m at a velocity higher than 15,000 km s^{-1} (Branch et al. 2007).

4.2. Inner Edge of Magnesium

Wheeler et al. (1998) identified the strong and relatively isolated absorption feature at $1.05\,\mu$m as Mg II $\lambda 1.0927\,\mu$m. The line is expected to be observed with decreasing velocity. The velocity is then expected to cease changing when the photosphere has receded below the inner edge of the Mg II distribution. Magnesium is a product of explosive carbon burning, but not oxygen burning, as the required higher temperatures for oxygen burning generate products further along the alpha chain, such as silicon and sulfur. This makes the Mg II line a sensitive probe to the location of the inner edge of carbon burning in velocity space (Wheeler et al. 1998; Marion et al. 2001, 2009; Höflich et al. 2002). Here, we focus on measuring the velocity using the location of the absorption minimum of the Mg II $\lambda 1.0927\,\mu$m line profile. With the NIR spectra of SN 2011fe and previous data from the literature, we explore the range of Mg II velocity and the accuracy limit of the velocity measurements.

The canonical Gaussian line profile is inadequate in fitting the Mg II P-Cygni profile, which contains influences from the P-Cygni wings of C I, O I and Si II. Using the Gaussian function to fit supernova line profiles often results in poor model fits which are unaccounted for by the errors. To properly estimate the uncertainties in the velocity measurements, we opted to use a principal component model which was built from data and empirically describes the variation in the line profiles. The formulation and the construction of the model are described in the Appendix.

The first four principal components and the model spectra, which account for over 90% of the variations, are plotted in Figure 7. The first two principal components, ξ_0 and ξ_1, show strong correlations between the strengths of the Mg II $\lambda\lambda 1.0092$, $1.0927\,\mu$m lines and the C I $\lambda 1.0693\,\mu$m line. These line strengths are also correlated with those of O I and Si III lines further to the red. The next principal component, ξ_2, describes approximately the varying tilts in the input spectra. Using these principal components, the model spectrum of the Mg II feature was then built as $M(\boldsymbol{p}, n)$, which varies as a function of the number of principal components n and the projections $\boldsymbol{p}$ onto the corresponding principal components.

To fit the observed spectrum, denoted by $O(\lambda)$ and with uncertainty $\Delta O(\lambda)$ and m wavelength elements, we allowed extra freedom in the model spectra $M(n, \boldsymbol{p})$ in the normalization
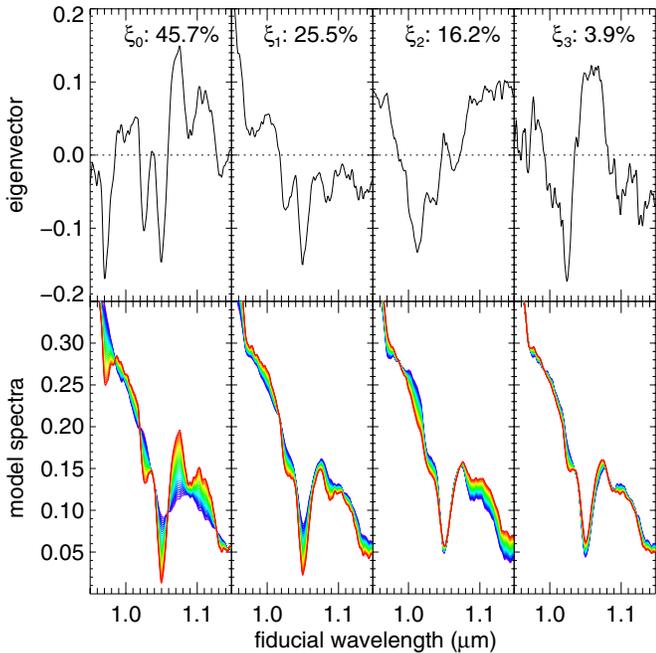
Figure 7. Principal component model of the region centered on the Mg II $\lambda 1.0927\,\mu$m line. The first four principal components are shown. For the model spectra, the effects of 1 σ variation in each projection p_j are shown. The eigenvalue for each principal component is noted on the top and is expressed as a fractional value, such that the sum of the N eigenvalues totals to 1. It is a measure of the amount of variation each principal component describes.

(A color version of this figure is available in the online journal.)

C and wavelength shift $\lambda_{\rm shift}$, and minimized the following:

$$\chi^2 = \sum_{i=0}^{m-1} \left[\frac{O_i(\lambda) - M\left(n, \boldsymbol{p}, C, \frac{\lambda_{\rm shift}}{1.05\,\mu{\rm m}}\lambda\right)}{\Delta O_i(\lambda)} \right]^2. \qquad (1)$$

The best fit model spectrum was determined using the IDL package `mpfit` (Markwardt 2009), a nonlinear least-squares fitting program ported from the FORTRAN package `MINPACK-1`. The number of principal components to include, n, was fixed in the fit and chosen, such that, the reduced χ^2 of the resulting best fit is closest to 1, typically $n = 6$–8.

Once the best-fit model spectrum was found, we attempted to remove the steep "continuum" with methods similar to that employed by Marion et al. (2009). A straight line connecting the model spectrum at fixed wavelengths to the blue and red side of best-fit $\lambda_{\rm shift}$ was taken as the continuum and removed from the model spectrum. The profile minimum of the continuum-removed model spectrum was then used to determine the line velocity of Mg II. The fit uncertainty of $\lambda_{\rm shift}$ was used to derive the measurement error for the velocity.

The Mg II velocities from several literature early-phase time-series NIR spectra were determined and plotted with the velocities of SN 2011fe in Figure 8. As predicted by Wheeler et al. (1998), SN 2011fe shows a rapid decrease in the Mg II line velocity followed by an extended epoch of constant velocity, beginning at ∼10 days before maximum and lasting until the feature disappears at ∼10 days past maximum. The velocity during this phase is remarkably constant for SN 2011fe, showing a dispersion of only 130 km s^{-1}, on the order of the velocity resolution of these medium-resolution spectra. The emission portion of the C I $\lambda 1.0693\,\mu$m P-Cygni profile is blended with

the absorption feature of Mg II $\lambda 1.0927\,\mu$m (Section 4.1). In the case of SN 2011fe, the time-varying characteristic of the C I feature had very little influence on the Mg II velocity during this epoch. For the rest of the SNe Ia in our sample, they appear to be caught after the Mg II line has entered the epoch of constant velocity, with the exception of the subluminous SN 1991bg-like SN 1999by. For SN 1999by, the Mg II velocity continues to decrease well past maximum light and indicates a distribution of Mg II down to ∼8,000 km s^{-1}. Note that SN 2002dj is a significant outlier in Figure 8 with exceptionally high Mg II velocity that persisted for a wide phase range before maximum light. SN 2002dj is also identified as a high velocity gradient object in the Benetti et al. (2005) classification (Pignata et al. 2008), similar to SN 2002bo (Benetti et al. 2004). The NIR spectrum of SN 2002bo also shows high Mg II velocity, although not as extreme as that of SN 2002dj. These results may point to a correspondence between high Si II velocity gradients and high Mg II velocities.

Here, we test whether the location of the inner edge of explosive carbon burning has a significant impact on the ^{56}Ni productions of SNe Ia. Using $\Delta m_{15}(B)$ (Phillips 1993) as a proxy for the amount of ^{56}Ni produced, the result is plotted in Figure 9. The Mg II velocity for each SN is the mean velocity, weighted by the measurement errors, in its constant epoch. The uncertainty is the intrinsic dispersion of the velocity around the mean during the constant epoch. For those SNe without adequate time-series data, the uncertainty is assumed to be the mean of the dispersions of all SNe Ia with time series, excluding SN 1999by.

There is a large spread in the locations of the inner edge of the Mg II distribution in SNe Ia. For a range of normal SNe Ia $1.0 < \Delta m_{15}(B) < 1.2$, the spread of Mg II velocities is as high as 5,000 km s^{-1}, as was observed by Marion et al. (2003, 2009). There appears to be no correlation between the Mg II velocity and $\Delta m_{15}(B)$. This result is surprising, since the transition density is expected to have a strong influence on the yield of ^{56}Ni (e.g., Höflich et al. 1995). The model of Höflich et al. (2002) for SN 1999by corresponds to the lowest transition density in the model grid. SN 1999by also happens to be a subluminous event and has very low Mg II velocities. Yet SN 2005am, with the next fastest decline rate in our sample, has one of the highest Mg II velocities measured. If the Mg II velocity is indeed a strong function of the transition density, its effect on the ^{56}Ni production and the brightness of SNe Ia appears to be secondary. Since its correlation to $\Delta m_{15}(B)$ is weak, it provides independent information which may affect the brightness of SNe Ia. We explore the possibility of using the Mg II velocity measurement to further improve the use of SNe Ia as distance indicators in Section 6.

4.3. H-band Iron-peak Feature

Soon past B-band maximum light, the NIR spectra take on a characteristic shape. Deep depression in regions between 1.2–1.5 μm is coupled with a dramatic feature between 1.5–1.9 μm, seemingly in emission (Figure 1). The feature was first noted by Kirshner et al. (1973). We now understand the deep depression as the result of a lack of line-blanketing opacity (Spyromilio et al. 1994). The early NIR spectra of SNe Ia are dominated by electron scattering. As the ejecta expand and cool, the electron scattering opacity decreases and, in turn, lowers the continuum flux level and exposes the core. In contrast, the strong line blanketing opacity from iron-peak elements causes the prominent feature at 1.5–1.9 μm to form at a larger effective radius and appear in emission (Wheeler et al. 1998).
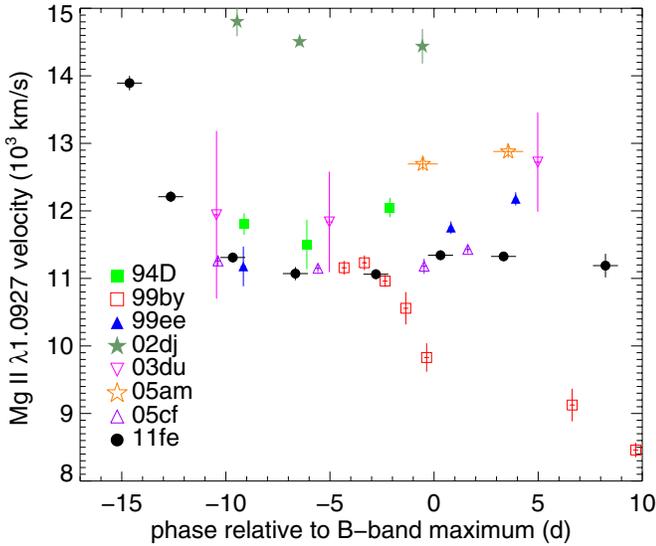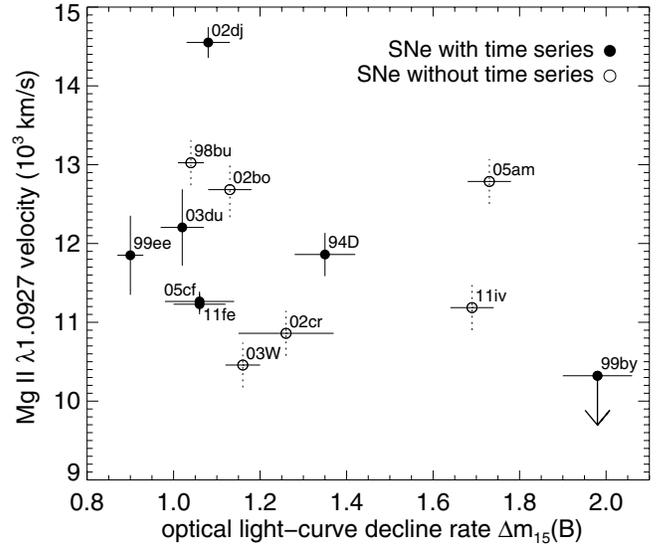
Figure 8. The time evolution of the Mg II $\lambda 1.0927\,\mu$m velocity.
(A color version of this figure is available in the online journal.)

Figure 9. The Mg II $\lambda 1.0927\,\mu$m velocity vs. optical light-curve decline rate $\Delta m_{15}(B)$. SNe Ia with three or more NIR spectra taken during the constant velocity epoch are plotted in filled circles, while the rest are plotted in open circles. For the peculiar SN 1999by, a downward arrow indicates that the constant velocity epoch has yet to be reached in the defined time interval (see Figure 8).

The strongly-variable opacity provides probes of very different depths at the same epoch. An alternate origin of the increased flux at 1.5–1.9 μm was proposed to be increased fluorescence in the region by Gall et al. (2012).

In the time-series data of SN 2011fe, we caught the budding of the prominent iron-peak feature in the spectrum at ∼3 days past B-band maximum (Figure 1). It then emerges rapidly to be the dominant feature in the NIR. This feature coincides in wavelength with the H band. The rapid time evolution and the shear size of the feature inevitably cause large uncertainties in the H-band k-corrections. Understanding the evolution and the diversity of the feature is crucial to control the systematic errors originating from k-correction estimates. The relative flux levels in regions of contrasting opacity also provide a temperature diagnostic for the line-blanketing material. Here, we explore the flux ratio across the break at 1.5 μm, which separates the different opacity regimes.

We define the H-band break ratio R as the ratio of the maximum flux just redward of the 1.5 μm break to the minimum flux just blueward of the 1.5 μm break (Figure 10). To determine the flux ratios for the sample of NIR spectra, the spectra were first smoothed with a Gaussian filter with a fixed width of $\Delta\lambda/\lambda = 0.0025$ in logarithmic wavelength space. The minima and maxima were found in fixed wavelength regions from the smoothed spectra. Since the velocity of the feature and the associated uncertainty do not enter in this analysis, we found that the Gaussian smoothing technique to be simpler and more robust than the PCA models described in Section 4.2. The measurement errors were estimated from the dispersions in the neighboring pixels, within ±100 Å, of the minima and maxima. The signal-to-noise ratio of each spectrum around the H-band break region is therefore reflected in the error. The resulting H-band break ratios for SN 2011fe and the sample of literature spectra are plotted in Figure 10. The H-band features of SNe Ia appear to emerge at very similar phases, ∼3 days past B-band maximum light. With the exception of the peculiar SN 1999by, the flux ratios appear to peak uniformly at ∼12 days past B-band maximum light; although, more time-series data are required to characterize the rise. Then, a remarkably uniform linear decline is observed among normal SNe Ia. Excluding the peculiar

SN 1999by, we determined an error-weighted mean linear decline of -0.146 day^{-1} with a standard deviation of 0.036 day^{-1}.

From our limited sample, the time evolution of the H-band break ratio R appears to be uniform with a range of values at peak. We defined R_{12} as the H-band break ratio at 12 days past B-band maximum. For each SN Ia with time-series data after the ratio peak, a straight line was fit to the linear post-peak decline. Then R_{12} was determined by extrapolating on the best-fit line to 12 days past B-band maximum. The uncertainty in R_{12} was derived from the error in the slope of the linear fit. For SNe Ia without adequate time-series data to determine the linear decline of the H-band break ratio, the error-weighted mean decline rate of -0.146 day^{-1} and an average uncertainty were adopted. The resulting R_{12} measurements are plotted against $\Delta m_{15}(B)$ in Figure 11.

The peak H-band Break ratio shows strong correlation with $\Delta m_{15}(B)$ (Figure 11); although, more time-series data are needed to confirm this finding. If the effect from intermediate-mass material at 1.2–1.5 μm is secondary, the correlation describes a temperature sequence. The temperature of the iron-peak material appears to be closely tied to the production of ^{56}Ni, more so than the transition density (Section 4.2). In the view point of contrasting opacity in the region, the observed effect can be explained as follows. At ∼12 days past B-band maximum, the electron scattering opacity is low enough that the iron-peak feature is fully exposed. The temperature of the iron-peak material now dictates the size of this feature. As the ejecta expands, the line-blanketing opacity drops with the decreasing temperature of the iron-peak material. The iron-peak feature at 1.5–1.9 μm then forms at decreasing effective radii and appears weaker. The uniformity of the time evolution indicates that the temperature decline of the iron-peak material is consistent in normal SNe Ia, regardless of the varying amounts of ^{56}Ni produced. The predictability of the strength and the evolution of the iron-peak feature means that we can indeed improve upon the current method of NIR k-correction (Hsiao et al. 2007; Hsiao 2009), by building, for example, spectral templates as a function of $\Delta m_{15}(B)$.
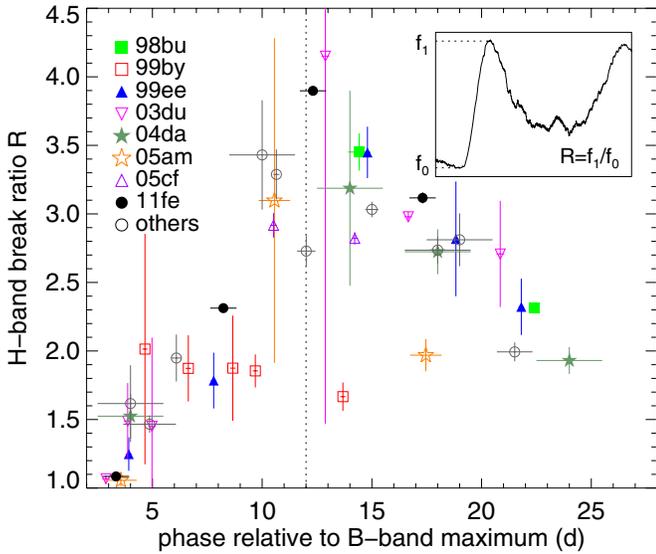
Figure 10. Time evolution of the ratio across the break at 1.5 μm R. The inset in the top right corner illustrates the definition of the break ratio with the spectrum SN 2011fe at 12.3 days past maximum.
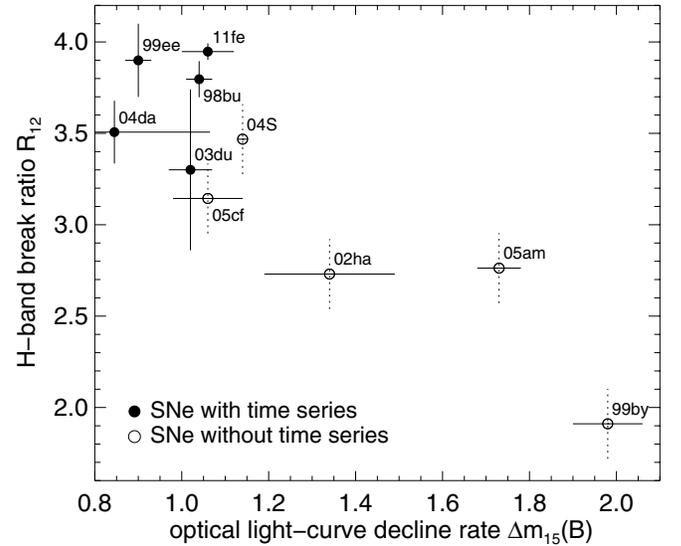
(A color version of this figure is available in the online journal.)

Figure 11. The ratio across the break at 1.5 μm at 12 days past maximum, R_{12}, vs. optical light-curve decline rate $\Delta m_{15}(B)$. SNe Ia with two or more time-series observations in the post-peak decline are plotted with filled circles, while the rest are plotted with open circles.

5. NIR K-CORRECTIONS

K-corrections account for the effect of cosmological expansion. SNe Ia at different redshifts would have their spectral energy distribution (SED) sampled at different wavelength regions by the same observed filter. A k-correction converts an observed magnitude to that which would be observed in the rest frame of the same or another filter, allowing for the comparison of the brightness of SNe Ia at various redshifts (Oke & Sandage 1968).[16] The calculation of k-corrections requires knowledge of the SED. While the effect of an assumed spectral template has been extensively studied in the optical (Nugent et al. 2002; Hsiao et al. 2007), the effect is not well understood in the NIR due to the relatively small spectroscopic sample (Hsiao 2009).

The current method of NIR k-corrections employs the revised spectral templates of Hsiao et al. (2007), warped to match the observed colors of the SN Ia (Burns et al. 2011). Here, we explore the effect of assuming the spectral template for the case of a SN 2011fe-like object at various redshifts. Before the k-corrections were calculated, the spectral template at each phase was warped to the NIR colors provided by WFCAM and WHIRC $izYJHK$ photometry of SN 2011fe (M. Im et al., in preparation; Matheson et al. 2012). The NIR spectra of SN 2011fe and the color-corrected spectral templates are plotted together for comparison in Figure 12.

The mismatch of the Mg II feature near 1.05 μm is evident in the first three spectra. The discrepancy is not surprising, since these are the earliest NIR spectra published to date. There also appears to be some mismatch in the strength of the prominent H-band feature at later phases. This illustrates the limitation of using a single template for all SNe Ia. As shown in Section 4.3, the strength of this iron-peak feature correlates with $\Delta m_{15}(B)$. Armed with this well-defined correlation, one can build a sequence of templates as a function of $\Delta m_{15}(B)$ to minimize the k-correction uncertainty associated with this feature.
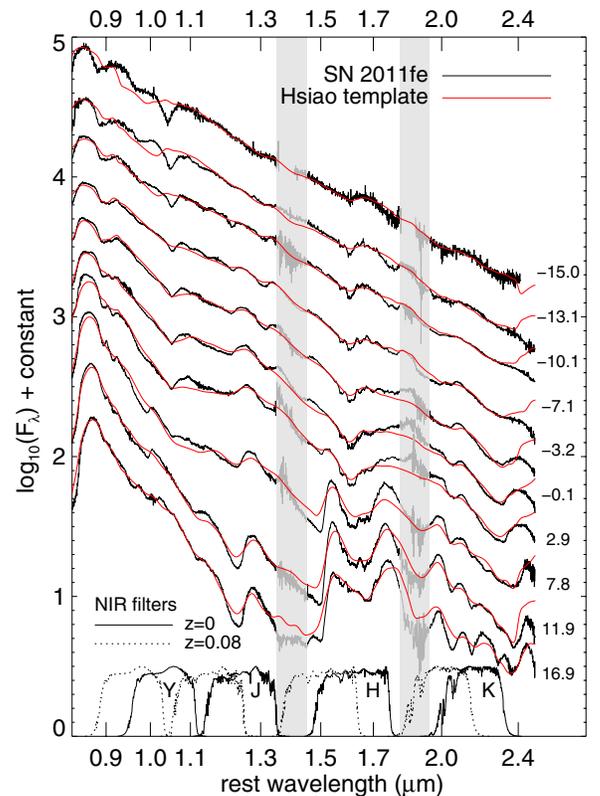

Figure 12. Comparison between the NIR spectra of SN 2011fe and the revised template of Hsiao et al. (2007) warped to match observed colors from $izYJHK$ photometry. At the bottom, the locations of the observed NIR filters at $z = 0$ and $z = 0.08$ are plotted in the rest frame of the supernova.

(A color version of this figure is available in the online journal.)

The mismatches between the spectra and template are reflected in the k-correction differences plotted in Figure 13. The k-correction differences were calculated at two redshifts, 0.03 and 0.08, which coincide with the redshift limits of current surveys of nearby SNe Ia in the Hubble flow. The larger differences observed at early phases in the Y band and at late phases in the

---

[16] See Aldering et al. (2002) for an alternative experimental approach that eliminates the need for k-corrections.
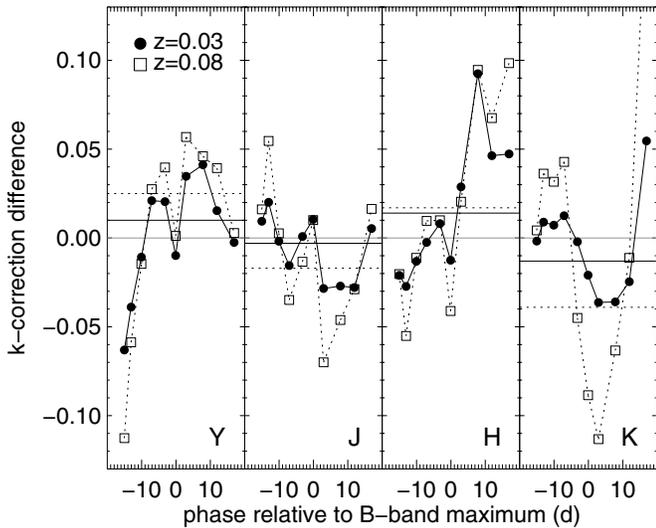
Figure 13. NIR *YJHK* *k*-correction difference between SN 2011fe and the revised template of Hsiao et al. (2007). Two redshifts are shown: $z = 0.03$ (filled circles and solid lines) and $z = 0.08$ (open squares and dotted lines). The horizontal lines mark the estimated offsets in the peak magnitude caused by the *k*-correction difference for $z = 0.03$ (solid lines) and $z = 0.08$ (dotted lines).

H band originate from the mismatches in the Mg II feature at early phases and the iron-peak feature at late phases. At $z = 0.08$ where the rest and observed filters are significantly misaligned, the mean absolute sizes of the differences over the phase range are 0.04, 0.03, 0.04, 0.06 mag in *Y, J, H, K*, respectively, similar to the numbers reported by Hsiao et al. (2007) for the optical filters. The offsets in the peak magnitude caused by assuming the spectral template can be approximated by using the average of the *k*-correction differences weighted by the light-curve template errors. For a SN 2011fe-like object, the impact of assuming a template SED on the determination of peak magnitude is small, on the level of 0.01 mag for $z = 0.03$ and 0.02–0.04 for $z = 0.08$ (Figure 13).

Nonetheless, whether the differences at various phases correlate with each other offers us important clues as to how to proceed to minimize the impact of uncertainties in *k*-corrections. If the *k*-correction differences from various phases are completely uncorrelated, more observations on the light curve could drive down the uncertainty in the peak magnitude determination. If the differences are significantly correlated, there is room for improvement in the time evolution of the spectral templates. The first attempt to quantify these correlations in the optical was made by Hsiao et al. (2007). This study requires a large sample of time-series spectra, which does not yet exist in the NIR. In Section 6, we describe the ongoing efforts to build such a data set.

The availability of color constraints from neighboring filters is also crucial for obtaining good *k*-correction estimates. For example, an accurate *k*-correction to the *J* band requires $Y - J$ and $J - H$ colors to warp the spectral template to the correct observed colors around the wavelength region in question. Missing color information inflates the *k*-correction uncertainty to ~0.1 mag (Hsiao et al. 2007). The higher *k*-correction difference seen in the *K* band in Figure 13 is most likely due to the lack of constraining observation in a redder band.

6. CONCLUSIONS

We have presented ten medium-resolution, high signal-to-noise ratio NIR spectra of SN 2011fe. This data set constitutes

the earliest time-series NIR spectroscopy of a SN Ia, with the first spectrum obtained at only 2.58 days past the explosion. We take advantage of these densely-sampled observations to gain insights into the time evolution and diversity of SN Ia NIR spectral features. The main findings are outlined below:

1. With the aid of the automated spectrum synthesis code SYNAPPS, C I $\lambda1.0693\,\mu$m is detected with increasing strength up to maximum light in SN 2011fe. The delay in its onset demonstrates the potential of the NIR C I line to be a superior tracer of unprocessed material to the more commonly used optical C II $\lambda0.6580\,\mu$m line.

2. The Mg II velocity of SN 2011fe, measured from the absorption minimum of the Mg II $\lambda1.0927\,\mu$m line profile, decreases rapidly at very early phases, then flattens to a remarkably constant evolution from 10 days before to 10 days past *B*-band maximum, with a dispersion of only 130 km s^{-1}.

3. Taking advantage of the constant velocity over a wide time window, the Mg II $\lambda1.0927\,\mu$m line, even without time-series observations, can be used to locate the inner edge of carbon burning. The Mg II profiles of SNe Ia exhibit a wide spread of velocities, as high as 5,000 km s^{-1}, and show no correlation with $\Delta m_{15}(B)$.

4. The prominent feature at 1.5–1.9 μm shows uniform phase evolution in SNe Ia. The flux ratio across the break at 1.5 μm increases from ~3 days past maximum, when the break appears, and reaches its peak at ~12 days past maximum. As a proxy for the temperature of the line-blanketing material, the strong correlation between the peak flux ratio and $\Delta m_{15}(B)$ indicates a close tie between temperature of the iron-peak elements and the production of ^{56}Ni.

5. Despite the presence of the prominent and rapidly-evolving feature at 1.5–1.9 μm near maximum light, the predictability of its strength and the evolution means that NIR *k*-corrections can be improved by producing spectral templates as a function of $\Delta m_{15}(B)$.

The result that the Mg II velocity does not correlate with $\Delta m_{15}(B)$ is an intriguing one, since the transition density is expected to have a strong influence on the yield of ^{56}Ni (e.g., Höflich et al. 1995). Is it possible that the Mg II velocity describes variations in SN Ia luminosity on a secondary level? Recently, SN Ia luminosity has been found to have a dependence on the host-galaxy stellar mass, in addition to the well-known dependence on light-curve shape and colors (e.g., Kelly et al. 2010; Sullivan et al. 2010; Lampeitl et al. 2010). It has been postulated that the effect may be attributed to the impact of progenitor metallicity on ^{56}Ni production (e.g., Timmes et al. 2003; Jackson et al. 2010). With the transition density linked to progenitor metallicity (Jackson et al. 2010), the NIR Mg II velocity is potentially a more direct probe of progenitor metallicity and a better calibrator of SN Ia luminosity than host-galaxy stellar mass.

With the limited size of the current NIR spectroscopic sample, the Mg II velocity shows a weak trend with the host-galaxy stellar mass, hinting a link of Mg II velocity to progenitor properties; although, a larger sample with unbiased host-galaxy properties is needed to determine if such a correlation indeed exists. To test whether the Mg II velocity provides better calibration of SN Ia luminosity than host-galaxy stellar mass, a statistical sample of NIR spectra, especially those of SNe Ia in the Hubble flow, is required. With improved NIR spectrographs available on large telescopes, obtaining NIR spectra of SNe Ia in the

Hubble flow is now feasible. For example, a pre-maximum NIR spectrum of SN 2012ar, a SN Ia with a recession velocity of 8472 km s^{-1}, was obtained in the low-resolution mode with the Folded-port Infrared Echellette (FIRE) on the 6.5 m Magellan Telescope. The spectrum reaches a signal-to-noise ratio of >50 at 1 μm, with an on-target integration time of only 10 minutes. With this signal-to-noise ratio, the measurement error for the Mg II velocity is still well below the intrinsic velocity dispersion of SN 2011fe in the constant velocity epoch (Section 4.2).

Throughout the paper, we have emphasized the need for an improved data set of NIR spectra to study this relatively unexplored area and to confirm the various findings from this paper. Starting in late 2011, we began a five-year program to build a large sample of high quality SN Ia NIR spectra using NIR spectrographs on large telescopes, such as FIRE, GNIRS and ISAAC (M. M. Phillips et al., in preparation). In the first year of the program, 130 NIR spectra have been obtained of 23 SNe Ia. The NIR time-series spectroscopy of SN 2011fe has demonstrated the many utilities of NIR spectra, both before and after maximum light, for both time-series and single "snapshot" observations. This improved data set will allow us to examine the efficacy of these tools and help to further decipher the nature of SNe Ia in the near future.

APPENDIX

PRINCIPAL COMPONENT MODEL LINE PROFILE

Principal component analysis (PCA) is a statistical technique useful for reducing the dimensionality and identifying patterns in a set of multi-dimensional data. We use the "bra ket" notation of Suzuki (2006) here for the formulation of PCA. A sample of early, high signal-to-noise ratio NIR spectra from the literature, including those of SN 2011fe, were used as PCA data input to build the model of the Mg II $\lambda 1.0927$ μm profile. Each spectrum was shifted in wavelength, such that the Mg II line minima coincide at a fiducial wavelength of 1.05 μm, normalized to the same integrated flux in the Y band, and interpolated into N fixed wavelength elements. The wavelength interval was chosen to be 10 Å, approximately matching and preserving the medium resolution of the SN 2011fe spectra at 1.05 μm. The log of the flux was used as the PCA input data and is denoted by $|m\rangle$. The mean spectrum $|\mu\rangle$ was computed and subtracted from the data set. A $N \times N$ covariance matrix was then computed to determine the strength of the correlation between spectral features.

The eigenvectors and eigenvalues of the covariance matrix were computed using internal IDL routines that utilize Householder reductions and the QL method (Press et al. 1992). Each of the N eigenvectors, or principal components, denoted here by $|\xi_j\rangle$, was ranked by the corresponding eigenvalue, which provides a measure of the amount of data variation the principal component describes. The zeroth-ranked principal component points in the direction of maximum variance in the N-dimensional data space, and subsequent principal components are orthogonal vectors:

$$\langle \xi_i | \xi_j \rangle = \delta_{ij}. \tag{A1}$$

Each of our input spectra can be expressed as the sum of the eigenvectors:

$$|m_i\rangle = |\mu\rangle + \sum_{j=0}^{N-1} p_{ij} |\xi_j\rangle, \tag{A2}$$

where p_{ij} is the projection of the ith input spectrum on the jth eigenvector.

Using these eigenvectors, the model spectrum of the Mg II feature was then built as $M(\boldsymbol{p}, n)$, which varies as a function of the number of eigenvectors $n \leqslant N$, and projection p_j for each eigenvector $|\xi_j\rangle$:

$$M(n, \boldsymbol{p}) = |\mu\rangle + \sum_{j=0}^{n-1} p_j |\xi_j\rangle. \tag{A3}$$

REFERENCES

Aldering, G., Adam, G., Antilogus, P., et al. 2002, Proc. SPIE, 4836, 61
Aspden, A. J., Bell, J. B., Day, M. S., Woosley, S. E., & Zingale, M. 2008, ApJ, 689, 1173
Barone-Nugent, R. L., Lidman, C., Wyithe, J. S. B., et al. 2012, MNRAS, 425, 1007
Benetti, S., Cappellaro, E., Mazzali, P. A., et al. 2005, ApJ, 623, 1011
Benetti, S., Meikle, P., Stehle, M., et al. 2004, MNRAS, 348, 261
Blondin, S., Matheson, T., Kirshner, R. P., et al. 2012, AJ, 143, 126
Bloom, J. S., Kasen, D., Shen, K. J., et al. 2012, ApJL, 744, L17
Bowers, E. J. C., Meikle, W. P. S., Geballe, T. R., et al. 1997, MNRAS, 290, 663

Branch, D., Baron, E., Hall, N., Melakayil, M., & Parrent, J. 2005, PASP, 117, 545
Branch, D., Garnavich, P., Geballe, T. R., et al. 2003, AJ, 126, 1489
Branch, D., Troxel, M. A., Jeffery, D. J., et al. 2007, PASP, 119, 709
Brown, P. J., Dawson, K. S., de Pasquale, M., et al. 2012, ApJ, 753, 22
Burns, C. R., Stritzinger, M., Phillips, M. M., et al. 2011, AJ, 141, 19
Chomiuk, L., Soderberg, A. M., Moe, M., et al. 2012, ApJ, 750, 164
Cushing, M. C., Vacca, W. D., & Rayner, J. T. 2004, PASP, 116, 362
Elias, J. H., Matthews, K., Neugebauer, G., & Persson, S. E. 1985, ApJ, 296, 379
Elias, J. H., Vukobratovich, D., Andrew, J. R., et al. 1998, Proc. SPIE, 3354, 555
Filippenko, A. V. 1982, PASP, 94, 715
Folatelli, G., Phillips, M. M., Burns, C. R., et al. 2010, AJ, 139, 120
Folatelli, G., Phillips, M. M., Morrell, N., et al. 2012, ApJ, 745, 74
Foley, R. J., Kromer, M., Howie Marion, G., et al. 2012, ApJL, 753, L5
Frogel, J. A., Gregory, B., Kawara, K., et al. 1987, ApJL, 315, L129
Gall, E. E. E., Taubenberger, S., Kromer, M., et al. 2012, MNRAS, 427, 994
Gamezo, V. N., Khokhlov, A. M., & Oran, E. S. 2004, PhRvL, 92, 211102
Gamezo, V. N., Khokhlov, A. M., Oran, E. S., Chtchelkanova, A. Y., & Rosenberg, R. O. 2003, Sci, 299, 77
Hamuy, M., Maza, J., Pinto, P. A., et al. 2002, AJ, 124, 417
Hernandez, M., Meikle, W. P. S., Aparicio, A., et al. 2000, MNRAS, 319, 223
Hicken, M., Challis, P., Jha, S., et al. 2009, ApJ, 700, 331
Höflich, P., Gerardy, C. L., Fesen, R. A., & Sakai, S. 2002, ApJ, 568, 791
Höflich, P., Khokhlov, A. M., & Wheeler, J. C. 1995, ApJ, 444, 831
Horesh, A., Kulkarni, S. R., Fox, D. B., et al. 2012, ApJ, 746, 21
Hoyle, F., & Fowler, W. A. 1960, ApJ, 132, 565
Hsiao, E. Y., Conley, A., Howell, D. A., et al. 2007, ApJ, 663, 1187
Hsiao, Y. C. E. 2009, PhD Thesis, Univ. of Victoria
Iwamoto, K., Brachwitz, F., Nomoto, K., et al. 1999, ApJS, 125, 439
Jackson, A. P., Calder, A. C., Townsley, D. M., et al. 2010, ApJ, 720, 99
Jha, S., Garnavich, P. M., Kirshner, R. P., et al. 1999, ApJS, 125, 73
Kasen, D. 2006, ApJ, 649, 939
Kasen, D., Röpke, F. K., & Woosley, S. E. 2009, Natur, 460, 869
Kattner, S., Leonard, D. C., Burns, C. R., et al. 2012, PASP, 124, 114
Kelly, P. L., Hicken, M., Burke, D. L., Mandel, K. S., & Kirshner, R. P. 2010, ApJ, 715, 743
Khokhlov, A. M. 1991, A&A, 245, 114
Khokhlov, A. M., Oran, E. S., & Wheeler, J. C. 1997, ApJ, 478, 678
Kirshner, R. P., Willner, S. P., Becklin, E. E., Neugebauer, G., & Oke, J. B. 1973, ApJL, 180, L97
Krisciunas, K., Garnavich, P. M., Stanishev, V., et al. 2007, AJ, 133, 58
Krisciunas, K., Marion, G. H., Suntzeff, N. B., et al. 2009, AJ, 138, 1584
Krisciunas, K., Phillips, M. M., & Suntzeff, N. B. 2004, ApJL, 602, L81
Kromer, M., & Sim, S. A. 2009, MNRAS, 398, 1809
Lampeitl, H., Smith, M., Nichol, R. C., et al. 2010, ApJ, 722, 566
Li, W., Bloom, J. S., Podsiadlowski, P., et al. 2011, Natur, 480, 348
Lynch, D. K., Rudy, R. J., Rossano, G. S., et al. 1990, AJ, 100, 223
Mandel, K. S., Narayan, G., & Kirshner, R. P. 2011, ApJ, 731, 120
Mandel, K. S., Wood-Vasey, W. M., Friedman, A. S., & Kirshner, R. P. 2009, ApJ, 704, 629
Margutti, R., Soderberg, A. M., Chomiuk, L., et al. 2012, ApJ, 751, 134
Marion, G. H., Höflich, P., Gerardy, C. L., et al. 2009, AJ, 138, 727
Marion, G. H., Höflich, P., Vacca, W. D., & Wheeler, J. C. 2003, ApJ, 591, 316

Marion, G. H., Höflich, P., & Wheeler, J. C. 2001, RMxAC, 10, 190
Marion, G. H., Höflich, P., Wheeler, J. C., et al. 2006, ApJ, 645, 1392
Markwardt, C. B. 2009, in ASP Conf. Ser. 411, Astronomical Data Analysis Software and Systems XVIII, ed. D. A. Bohlender, D. Durand, & P. Dowler (San Francisco, CA: ASP), 251
Matheson, T., Joyce, R. R., Allen, L. E., et al. 2012, ApJ, 754, 19
Meikle, W. P. S., Cumming, R. J., Geballe, T. R., et al. 1996, MNRAS, 281, 263
Niemeyer, J. C., & Woosley, S. E. 1997, ApJ, 475, 740
Nomoto, K., Sugimoto, D., & Neo, S. 1976, Ap&SS, 39, L37
Nomoto, K., Thielemann, F.-K., & Yokoi, K. 1984, ApJ, 286, 644
Nugent, P., Kim, A., & Perlmutter, S. 2002, PASP, 114, 803
Nugent, P., Phillips, M., Baron, E., Branch, D., & Hauschildt, P. 1995, ApJL, 455, L147
Nugent, P. E., Sullivan, M., Cenko, S. B., et al. 2011, Natur, 480, 344
Oke, J. B., & Sandage, A. 1968, ApJ, 154, 21
Parrent, J. T., Howell, D. A., Friesen, B., et al. 2012, ApJL, 752, L26
Parrent, J. T., Thomas, R. C., Fesen, R. A., et al. 2011, ApJ, 732, 30
Patat, F., Cordiner, M. A., Cox, N. L. J., et al. 2013, A&A, 549, A62
Perlmutter, S., Aldering, G., Goldhaber, G., et al. 1999, ApJ, 517, 565
Phillips, M. M. 1993, ApJL, 413, L105
Pignata, G., Benetti, S., Mazzali, P. A., et al. 2008, MNRAS, 388, 971
Pinto, P. A., & Eastman, R. G. 2000, ApJ, 530, 757
Plewa, T., Calder, A. C., & Lamb, D. Q. 2004, ApJL, 612, L37
Press, W. H., Teukolsky, S. A., Vetterling, W. T., & Flannery, B. P. 1992, Numerical Recipes in C. The Art of Scientific Computing (2nd ed.; Cambridge: Cambridge Univ. Press)
Rayner, J. T., Toomey, D. W., Onaka, P. M., et al. 2003, PASP, 115, 362
Riess, A. G., Filippenko, A. V., Challis, P., et al. 1998, AJ, 116, 1009
Röpke, F. K., Hillebrandt, W., Schmidt, W., et al. 2007, ApJ, 668, 1132
Röpke, F. K., Kromer, M., Seitenzahl, I. R., et al. 2012, ApJL, 750, L19
Silverman, J. M., & Filippenko, A. V. 2012, MNRAS, 425, 1917
Spyromilio, J., Meikle, W. P. S., Allen, D. A., & Graham, J. R. 1992, MNRAS, 258, 53P
Spyromilio, J., Pinto, P. A., & Eastman, R. G. 1994, MNRAS, 266, L17
Stanishev, V., Goobar, A., Benetti, S., et al. 2007, A&A, 469, 645
Sullivan, M., Conley, A., Howell, D. A., et al. 2010, MNRAS, 406, 782
Suzuki, N. 2006, ApJS, 163, 110
Tanaka, M., Mazzali, P. A., Benetti, S., et al. 2008, ApJ, 677, 448
Thomas, R. C., Aldering, G., Antilogus, P., et al. 2007, ApJL, 654, L53
Thomas, R. C., Aldering, G., Antilogus, P., et al. 2011a, ApJ, 743, 27
Thomas, R. C., Nugent, P. E., & Meza, J. C. 2011b, PASP, 123, 237
Timmes, F. X., Brown, E. F., & Truran, J. W. 2003, ApJL, 590, L83
Toth, I., & Szabó, R. 2000, A&A, 361, 63
Vacca, W. D., Cushing, M. C., & Rayner, J. T. 2003, PASP, 115, 389
Vinkó, J., Sárneczky, K., Takts, K., et al. 2012, A&A, 546, A12
Wheeler, J. C. 2012, ApJ, 758, 123
Wheeler, J. C., Hoeflich, P., Harkness, R. P., & Spyromilio, J. 1998, ApJ, 496, 908
Wood-Vasey, W. M., Friedman, A. S., Bloom, J. S., et al. 2008, ApJ, 689, 377
Woosley, S. E., Kerstein, A. R., & Aspden, A. J. 2011, ApJ, 734, 37
Woosley, S. E., Kerstein, A. R., Sankaran, V., Aspden, A. J., & Röpke, F. K. 2009, ApJ, 704, 255
Yamaoka, H., Nomoto, K., Shigeyama, T., & Thielemann, F.-K. 1992, ApJL, 393, L55